

# Geophysical Research Letters<sup>®</sup>

## RESEARCH LETTER

10.1029/2021GL095117

Ryo Okuwaki and Stephen P. Hicks contributed equally to this work.

### Key Points:

- A moment magnitude 7.3 2021 East Cape, New Zealand intraslab earthquake comprised multiple rupture episodes with different faulting styles
- The complex rupture comprises components of shallow trench-normal extension and unexpectedly, deep trench-parallel compression in slab
- The trench-parallel compression likely reflects stress rotation at a buoyancy contrast that drives slab contortion

### Supporting Information:

Supporting Information may be found in the online version of this article.

### Correspondence to:

R. Okuwaki,  
rokuwaki@geol.tsukuba.ac.jp






### Citation:

Okuwaki, R., Hicks, S. P., Craig, T. J., Fan, W., Goes, S., Wright, T. J., & Yagi, Y. (2021). Illuminating a contorted slab with a complex intraslab rupture evolution during the 2021 Mw 7.3 East Cape, New Zealand earthquake. *Geophysical Research Letters*, 48, e2021GL095117. <https://doi.org/10.1029/2021GL095117>

Received 14 JUL 2021  
Accepted 10 DEC 2021

© 2021. American Geophysical Union.  
All Rights Reserved.

## Illuminating a Contorted Slab With a Complex Intraslab Rupture Evolution During the 2021 Mw 7.3 East Cape, New Zealand Earthquake

Ryo Okuwaki<sup>1,2,3</sup> , Stephen P. Hicks<sup>4</sup> , Timothy J. Craig<sup>3</sup> , Wenyan Fan<sup>5</sup> , Saskia Goes<sup>4</sup> , Tim J. Wright<sup>3</sup> , and Yuji Yagi<sup>2</sup> 

<sup>1</sup>Mountain Science Center, University of Tsukuba, Tsukuba, Japan, <sup>2</sup>Faculty of Life and Environmental Sciences, University of Tsukuba, Tsukuba, Japan, <sup>3</sup>COMET, School of Earth and Environment, University of Leeds, Leeds, UK, <sup>4</sup>Department of Earth Science and Engineering, Imperial College London, London, UK, <sup>5</sup>Scripps Institution of Oceanography, UC San Diego, La Jolla, CA, USA

**Abstract** The state-of-stress within subducting oceanic plates controls rupture processes of deep intraslab earthquakes. However, little is known about how the large-scale plate geometry and the stress regime relate to the physical nature of the deep intraslab earthquakes. Here we find, by using globally and locally observed seismic records, that the moment magnitude 7.3 2021 East Cape, New Zealand earthquake was driven by a combination of shallow trench-normal extension and unexpectedly, deep trench-parallel compression. We find multiple rupture episodes comprising a mixture of reverse, strike-slip, and normal faulting. Reverse faulting due to the trench-parallel compression is unexpected given the apparent subduction direction, so we require a differential buoyancy-driven stress rotation, which contorts the slab near the edge of the Hikurangi plateau. Our finding highlights that buoyant features in subducting plates may cause diverse rupture behavior of intraslab earthquakes due to the resulting heterogeneous stress state within slabs.

**Plain Language Summary** A key type of tectonic boundary is where two plates collide with one sinking into the mantle beneath. These subduction zones generate the world's largest earthquakes. Quantifying stress in the subducting plate ("slab") is important because slabs drive the global plate-tectonic system, and large earthquakes can occur within them. These earthquakes can cause strong shaking, and when occurring near cities, can lead to damage. However, mapping stress is challenging as we cannot directly "see" inside deep slabs. Our best indications of slab stress come from earthquakes themselves. A magnitude 7.3 earthquake north of New Zealand in 2021 generated a distinct pattern of seismic waveforms at seismometers installed worldwide. We used these seismic records to probe the earthquake, providing a new view of stress in subduction zones. We found the earthquake generated both vertical and horizontal motions along faults, driven by compressional and extensional stresses deep within the slab. The compressional part is oriented 90 degrees from the subduction direction, which is opposite to the usual compression in subduction zones. This unusual direction of compression can be explained by subduction of a thickened and buoyant part of the Pacific plate, known as the Hikurangi plateau.

## 1. Introduction

Complex fault configurations and heterogeneous fault conditions, that is, stress and strength states, govern earthquake rupture development and propagation (Avouac et al., 2014; Elliott et al., 2016; Floyd et al., 2016; Hamling et al., 2017). Such relations can be inferred from the fault geometry and long-term geodetic observations for shallow active faults (Arai et al., 2016; Elliott et al., 2016; Hamling et al., 2017; Hayes et al., 2018; Simons et al., 2002; Sippl et al., 2018; Williams et al., 2013). However, for intraslab earthquakes occurring below ~50 km depth, these physical controlling factors are difficult to assess because of challenges to map the structure at such depths and the general lack of seismicity there (Dascher-Cousineau et al., 2020; Gomberg & Bodin, 2021; Page et al., 2016; Ranero et al., 2005; Wiens, 2001). In particular, the internal stress state and its extensional-compression transition regime are often elusive in subducted slabs, although they directly impact intraslab earthquake occurrence and their faulting styles (Ammon et al., 2008; Astiz et al., 1988; Craig et al., 2014; Romeo & Álvarez-Gómez, 2018; Sandiford et al., 2019, 2020; Ye et al., 2021). Thus, imaging the rupture processes of large, deep intraslab earthquakes offers a rare window to investigate the slab configuration and to understand fault

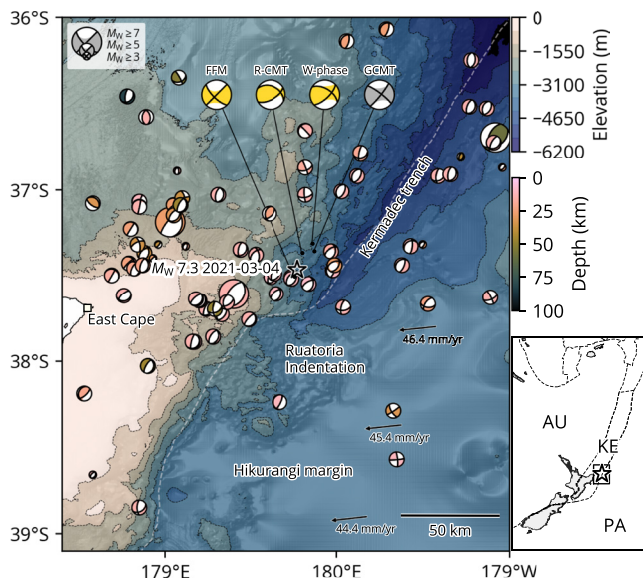


**Figure 1.** Seismotectonic overview of the study region in the north of East Cape, New Zealand. The star shows the relocated hypocenter of the  $M_w$  7.3 2021 East Cape earthquake. Beach balls are the lower-hemisphere stereographic projection of the moment tensor solutions before the 2021 East Cape earthquake, colored by depth (Dziewonski et al., 1981; Ekström et al., 2012). Yellow beach balls are the moment tensor solutions for the 2021 East Cape earthquake obtained by this study (FFM; Finite-fault model, R-CMT; regional centroid-moment tensor (CMT), and W-phase; W-phase moment tensor). Background contours display bathymetry (Mitchell et al., 2012). The arrows show the relative plate motions with the convergence rate of the Pacific plate (PA) towards the fixed Australian plate (AU) (DeMets et al., 2010). The dashed line gives the approximate location of the subduction trench (e.g., Bassett et al., 2010). The right map shows the wider setting of the study region. The rectangle shows the area of the left map. The star marks the epicenter. The dashed lines are the plate boundaries (Bird, 2003) between the Pacific (PA), the Australian (AU), and the Kermadec (KE) plates.

interaction and rupture evolution of these earthquakes, illuminating heterogeneous stress fields.

An intraslab moment magnitude ( $M_w$ ) 7.3 earthquake occurred offshore the East Cape in northern New Zealand on 4 March 2021, which was followed  $\sim 4$  hr later by a series of the  $M_w$  7.4 and  $M_w$  8.1 earthquakes in the Kermadecs ( $\sim 900$  km to the north) (GeoNet, 2021). The  $M_w$  7.3 2021 East Cape earthquake, which is the focus of this paper, may offer insight into the regional slab geometry because of its location and complex rupture process. The 2021 East Cape earthquake locates at the boundary between the southern end of Kermadec trench and the northern end of Hikurangi margin, where the Pacific plate subducts beneath the Australian plate and its convergence decreases and progressively rotates to oblique motion toward the south (Figure 1) (Collot et al., 1996, 2001; Lewis et al., 1998; Wallace et al., 2009). The earthquake produced observable tsunami signals at tide gauges at the northern coast of New Zealand (GeoNet News, 2021), indicating seafloor deformation due to possible shallow slip. However, the reported centroid depth of the earthquake was  $\sim 50$  km (Duputel et al., 2012; Dziewonski et al., 1981; Ekström et al., 2012; U.S. Geological Survey Earthquake Hazards Program, 2017), and the focal mechanism indicates oblique-thrust motion, with the compressional axis oriented toward the north-south direction (Figure 1) (U.S. Geological Survey Earthquake Hazards Program, 2017; Duputel et al., 2012; Dziewonski et al., 1981; Ekström et al., 2012). This compressional axis suggests the earthquake was not a simple shallow normal- or reverse-faulting event with the strike angle oriented parallel to the trench axis, as is typically seen in many subduction zones (Figure 1) (Duputel et al., 2012; Dziewonski et al., 1981; Ekström et al., 2012; U.S. Geological Survey Earthquake Hazards Program, 2017). All these apparently inconsistent observations (GeoNet, 2021; GeoNet News, 2021) suggest a complex rupture process of the East Cape earthquake, possibly involving multiple faults at different depths.

Although the subduction-related deformation processes in the region south of East Cape have received a lot of scientific attention (e.g., Eberhart-Phillips & Reyners, 1999; Mochizuki et al., 2021; Reyners et al., 2006; Wallace et al., 2009), the transition to the Tonga-Kermadec arc is less well understood.

In the region north of East Cape, sporadic deep seismicity ( $>80$ -km depth) contrasts with abundant shallow seismicity ( $<50$ -km depth) (Dziewonski et al., 1981; Ekström et al., 2012; GeoNet, 2021; GeoNet Moment Tensors, 2021; U.S. Geological Survey Earthquake Hazards Program, 2017). Most of the shallow earthquakes are normal faulting events within the top of the oceanic plate due to trench-normal extensional stress due to slab bending into the trench (Bassett et al., 2010; Henrys et al., 2006; Reyners & McGinty, 1999). With these shallow earthquakes, the plate interface and the surrounding materials have been imaged down to  $\sim 20$  km depth (Bassett et al., 2010, 2016; Bell et al., 2010; Davey et al., 1997), but the lithospheric structure of the deep slab is poorly resolved. The apparent complex rupture process of the 2021 East Cape earthquake offers a unique opportunity to infer the stress regime associated with the deeper subduction process.

Here, we show that the rupture process of the 2021 East Cape earthquake involves multiple rupture episodes that can be fitted with a mixture of reverse, strike-slip, and normal faulting mechanisms. These episodes ruptured multiple faults through the subducted oceanic lithosphere at various depths. The earthquake initiated at approximately 70 km depth with an unexpected trench-parallel compressional reverse faulting mechanism, and followed by a slip episode at about 30 km depth, which is likely governed by more usual slab-bending trench-normal downdip extension. Such a rupture process reflects a heterogeneous stress regime within the subducted slab, in response to a possible geometric change of the slab in-depth due to either the subduction of a seamount associated with the Ruatoria debris slide (Collot et al., 2001; Lewis et al., 1998, 2004) or a sharp change in slab buoyancy at the northern end of the subducting Hikurangi oceanic plateau.

## 2. Hypocenter, Aftershock Relocation, and Initial Source Estimates

We first determined the hypocenter of the East Cape earthquake by nonlinear inversion of *P*- and *S*-wave arrival times at regional distances using a 1D velocity model appropriate for the region north of East Cape (Text S1; Figure S1 in Supporting Information S1). Our relocated epicenter lies along the trench axis, is within 10 km of the GeoNet solution (GeoNet, 2021), and ~35 km ENE of the U.S. Geological Survey National Earthquake Information Center (USGS-NEIC) solution (U.S. Geological Survey Earthquake Hazards Program, 2017), which is consistent with the USGS-NEIC epicenters being systematically shifted to the downdip direction in subduction zones (e.g., Ye et al., 2017). Our maximum likelihood hypocenter depth is 72 km. Although this hypocenter depth may be thought to be inherently uncertain due to the suboptimal station coverage, it provides an initial hypothesis for testing our results of the more complex rupture configuration later. If we instead fix our hypocentral depth at the fixed GeoNet/USGS estimates of 10–12 km (GeoNet, 2021; U.S. Geological Survey Earthquake Hazards Program, 2017), the root-mean-square (RMS) residual of arrival times at the closest stations (<200 km) increases by 0.3 s. Although the deeper hypocentral depth led to lower RMS value, the lower RMS value only represents a better data fit and does not reduce the nonuniqueness of the inverse problem, hence not equivalent to location uncertainty itself. The 68% confidence ellipsoid of our solution corresponds to an epicentral uncertainty of 0.03° and 0.02° in longitude and latitude, respectively; the depth uncertainty is ±9 km (Figure S1 in Supporting Information S1). However, no depth phases were reported in the International Seismological Centre Bulletin for this earthquake (International Seismological Centre, 2021), presumably due to interference with the long source-time function.

Next, we located aftershocks of the 2021 East Cape earthquake the same way as for the mainshock. We focus on events reported by GeoNet (2021) occurring from 4 March 2021 to 11 April 2021 (1 week from the mainshock); (Figure S2 in Supporting Information S1), which yields 622 events with magnitudes ranging from 1.5 to 6.2. To assure the robustness of the solutions, we remove earthquakes and their arrivals that (a) were not manually reviewed by GeoNet (2021), (b) have maximum azimuthal gaps of more than 295 degrees, and (c) have fewer than at least 10 phase arrivals (Figure S2 in Supporting Information S1). The median depth uncertainty of these aftershocks is 22 km (with 6 km standard deviation), and the median epicentral uncertainties are 0.05° and 0.08° in latitude and longitude, respectively. The aftershocks suffer large depth uncertainty due to their location outside of the regional network, which hampers an unambiguous determination of the total rupture area. However, we broadly identify both shallow (<30 km) and deep (>50 km) aftershocks, and such a depth distribution could be explained by our preferred rupture model of both shallow and deep ruptures in the downgoing lithosphere.

Using a Bayesian bootstrapping CMT inversion of low-frequency (2.0–8.5 mHz) teleseismic waveforms for a single-point source (Text S2 in Supporting Information S1), we find a mean centroid depth of 53 km, with a centroid position shifted 18 km NNE of our relocated epicenter, and time shift from the origin time of +5 s (Figure S3 in Supporting Information S1). However, the CMT solution has a large non-double couple component (DC = 15%). Such a low DC component is likely caused by geometric complexities of the earthquake that may involve multiple faults within the subducted Pacific plate near the Hikurangi trench.

Finally, to test the hypothesized rupture complexity, we investigated the rupture process of the earthquake with a multi-point CMT (R-CMT) inversion method using regional seismic waveforms (Text S3; Figures S4–S6 in Supporting Information S1). The approach can resolve the first-order features of a complex rupture with few assumptions. The later part of the <25 s period surface waves on the horizontal components at stations within ~400 km epicentral distance are poorly fit (Figures S5 and S6 in Supporting Information S1) due to basin resonance effects (Kaneko et al., 2019). We find that the East Cape event can be best explained by two sub-events, with the largest sub-event ( $M_w \sim 7.3$ ) at 50–70 km depth occurring 8–10 s after the origin time, and the second sub-event at 7–12 km depth and 6–8 s after the first sub-event. The second sub-event significantly increases waveform variance reduction (VR) by 16%–23%. The first sub-event has an oblique-reverse mechanism. Conversely, the second sub-event has a normal faulting mechanism. Overall, our R-CMT solution corroborates a complex rupture scenario involving at least two sub-events separated by ~40 km in depth: one at the top of the Pacific plate and the other deep within the slab.

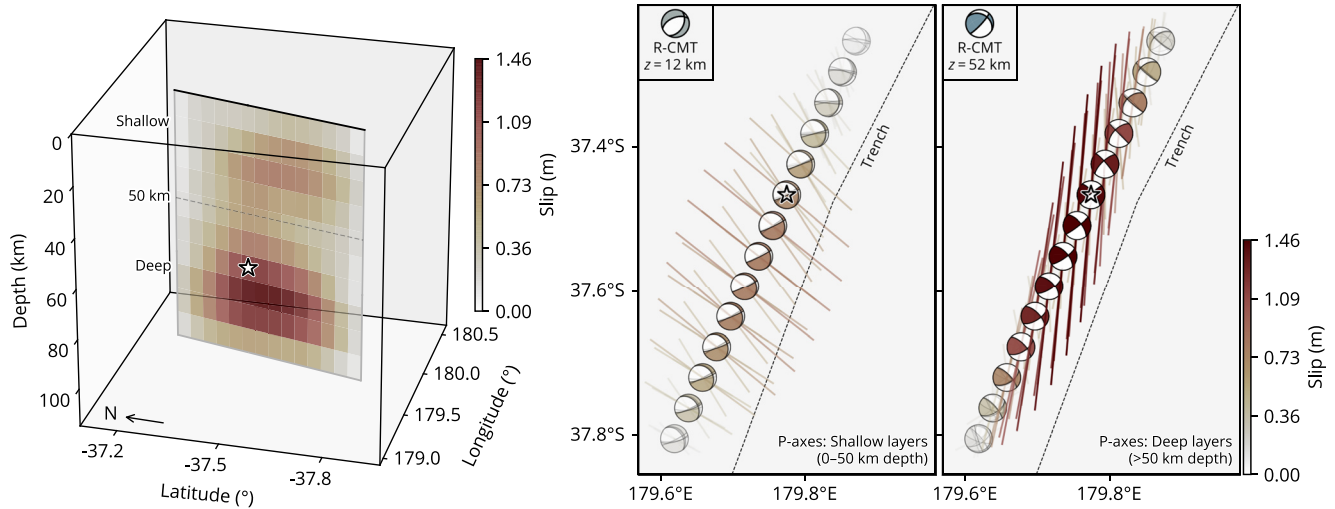


**Figure 2.** Static slip distribution. The left panel shows the total slip distribution in 3D view, viewed from the southwest. The star represents our hypocenter. The black line shows the top of the model fault. The right panels show the map view of the slip distribution from shallow (<50 km) and deep depths ( $\geq 50$  km), with beach balls representing double-couple components of the moment tensor solution (Figure S7 in Supporting Information S1), and corresponding P-axis azimuths (bars scaled by slip). The moment tensor is calculated by integrating the slip-rate function for each basis component of moment tensor with respect to time at each subfault. The P-axis azimuth is extracted from the resultant double-couple solution for each sub-fault, which is represented by a lower-hemisphere stereographic projection. We show the beach ball from the slip patch corresponding to the fault element with the maximum slip within each given depth range. The inset shows the corresponding R-CMT solutions annotated with their depths ( $z$ ). The dashed line is the subduction trench (Bird, 2003).

### 3. Intermittent Complex Multiple Rupture Episodes With Various Focal Mechanisms

To better understand the rupture development, we applied a finite-fault potency-density inversion method (Shimizu et al., 2020) to estimate the rupture evolution of the 2021 East Cape earthquake (Text S4 in Supporting Information S1). The method can flexibly accommodate multiple faults with different geometries rupturing during the same event, which are inferred from the spatiotemporal distribution of five-basis double-couple components of the potency-density tensors (Ampuero & Dahlen, 2005; Kikuchi & Kanamori, 1991). In our inversion formulation, the model parameters are objectively determined by minimizing Akaike's Bayesian Information Criterion (ABIC) (Akaike, 1980; Yabuki & Matsu'ura, 1992), and we do not adopt non-negative constraints for slip vectors. Such a procedure can effectively prevent over- or under-smoothing of the source model as theoretically shown in Fukuda and Johnson (2008). Particularly, we flexibly solve the potency density in a finite-fault domain instead of regularizing the model with possible inaccurate subjective assumptions (e.g., positivity constraints and the prescribed fault geometry). The method has proven effective at resolving complex earthquake ruptures in a variety of tectonic settings (Hicks et al., 2020; Okuwaki et al., 2020; Shimizu et al., 2020, 2021; Tadapansawut et al., 2021; Yamashita et al., 2021). In practice, we parameterize a 2D vertical model domain along a  $200^\circ$  strike extending from 7- to 107-km depth with a total of 140 source elements (subfaults) (Figure 2). This parameterization is guided by the observed cluster of the near-trench-parallel aftershocks (Figure S2 in Supporting Information S1). Although it is difficult to resolve the absolute locations of slip surfaces due to insufficient spatial resolution of the teleseismic body waves used in our finite-fault modeling, in the 2D model domain, we solve the fault-normal and shear-slip vectors at each source element, which are independent of the model domain geometry. In other words, we solve for distributed sources in the model domain that may have any type of faulting mechanism required by the data. The model domain therefore allows multiple faulting episodes of the earthquake and does not necessarily indicate a single fault plane cutting through the lithosphere in a continuous rupture. Our preferred slip model suggests that the earthquake initiated at 72 km depth (Figure S12 in Supporting Information S1), which yields VR of waveform fitting 74% corroborating the relocated hypocenter and the R-CMT solution. We test possible model domain geometries that only cover some specific depths, but the finite-fault models of such model setups cannot adequately explain the observed waveforms (Figure S12 in Supporting Information S1). We note that a 3-D parameterization would have been ideal for imaging this earthquake, but it is currently infeasible due to computational limits.



To further test our model, we also use the same data set and model domain to invert a finite-fault model but restrict the subfaults to have the same strike and dip (Figure S14 in Supporting Information S1). The results of our test show that in comparison to our preferred finite-fault model, fixing the focal mechanisms to the prescribed model plane has a much lower VR of 25%. This exercise highlights the importance of permitting a complex rupture scenario when modeling this earthquake and shows that an overly simplified model would fail to explain even the first few seconds of the direct  $P$  waves (for example, first 5 s  $P$  waves of XMAS and CRZF stations). These early  $P$  waves are unlikely to be affected by water phases given the source depth. The water multiples should be incoherent with azimuth, given the variation in water depth around the source region. Such incoherent phases that are not represented in the Green's functions used in our inversion cannot translate into complexity in source time function. We also note that using a 1D velocity model for Green's functions without considering the simplification effects may introduce erroneous biases. Further, even using 3D velocity models to compute the Green's functions, the fidelity of the velocity models remains a source of uncertainty. For example, the local 3D velocity model (e.g., Eberhart-Phillips et al., 2010, 2020) may suffer uncertainties for the area near the 2021 event because of a lack of offshore stations for tomographic inversions. Our approach can address such assumption-induced errors. We explicitly consider these effects by introducing an uncertainty term of the Green's function into the data covariance matrix in the inversion formulation (Yagi & Fukahata, 2011). Such an approach has proven effective in reducing solution errors that are due to model oversimplifications (Duputel et al., 2014; Minson et al., 2013; Ragon et al., 2018; Yagi & Fukahata, 2011).

Our preferred finite-fault model suggests that most of the slip occurred at 55–100 km depth and ~15 km south of the hypocenter, releasing 69% of the total moment (Figure 2). Another patch of slip is observed at 20–40 km depth, much shallower than the hypocentral depth and comprising 31% of the total moment. The deeper slip is dominated by an oblique strike-slip faulting mechanism. The shallow slip involves a mixture of normal and strike-slip faulting mechanisms. The finite-fault model leads to a moment estimate of  $1.7 \times 10^{20}$  Nm ( $M_w$  7.4). We evaluated the robustness and uncertainty of the finite-fault model by performing synthetic tests (Figure S13 in Supporting Information S1). The result shows that both the slip pattern and the variation of faulting mechanism in the model domain are well reproduced. We will discuss in detail in a later section, but the focal mechanisms of the shallow and deep domains agree with the R-CMT solutions (Figure 2), which show shallow normal faulting with the likely fault plane striking parallel to the trench axis and deep reverse faulting with the compressional axis orienting along the trench axis.

The rupture process of the East Cape earthquake involved deep- and shallow-slip corresponding to different faulting types, which may be expressed as a few bursts of rupture episodes (e.g., E1 to E4). In this interpretation, the earthquake initiated as reverse faulting with a strike-slip component for the first 5 s (E1, Figure 3). The rupture then propagated toward the south at 60–100 km depth, releasing 20% of the total moment and lasting for about 5 s (E2, Figure 3). This episode was dominated by reverse faulting. The third episode (E3) simultaneously might have ruptured several fault patches from 5 to 15 s, including a shallow patch at ~25 km depth and a deep patch at ~70 km depth (Figure 3). The shallow part of E3 ruptured with a normal faulting mechanism, while the deep patch of E3 had a strike-slip mechanism. The last major episode (E4) ruptured a fault patch beneath the hypocenter for about 5 s with a dominant strike-slip focal mechanism (Figure 3). We note that E4 is unique as its dominant mechanism suggests a strike-slip faulting style, while the E1 and E2 show reverse mechanisms (Figure 3). The remaining 26% of the total moment was released by slips at both shallow and deep regions, and the earthquake lasted for about ~30 s. Most of the seismic moment was released within ~20 s in our finite-fault solution, consistent with the half-duration of the GCMT solution (10 s) (Dziewonski et al., 1981; Ekström et al., 2012), which seems typical as for other similar-sized earthquakes (e.g., Duputel et al., 2013).

The four rupture episodes appear compact in size and seem to involve multiple faulting mechanisms at different depths. Given the varying focal mechanisms, the chaotic episodes likely do not result from the same continuous rupture front, but more likely represent segmented slip on different faults that may have interacted with, and triggered, each other.

Our preferred finite-fault solution suggests a non-uniform moment release of the earthquake, which could be due to spatiotemporally disconnected rupture episodes (Figures 3 and S15 in Supporting Information S1). Alternatively, the results could also represent two sub-events with longer durations. In this case, the deep sub-event initiates at the hypocenter and propagates toward south at <2.5 km/s until 15 s from the origin. The higher slip rate, seen during 15–20 s located around the hypocenter, can be as a result of faster <5 km/s back-propagation

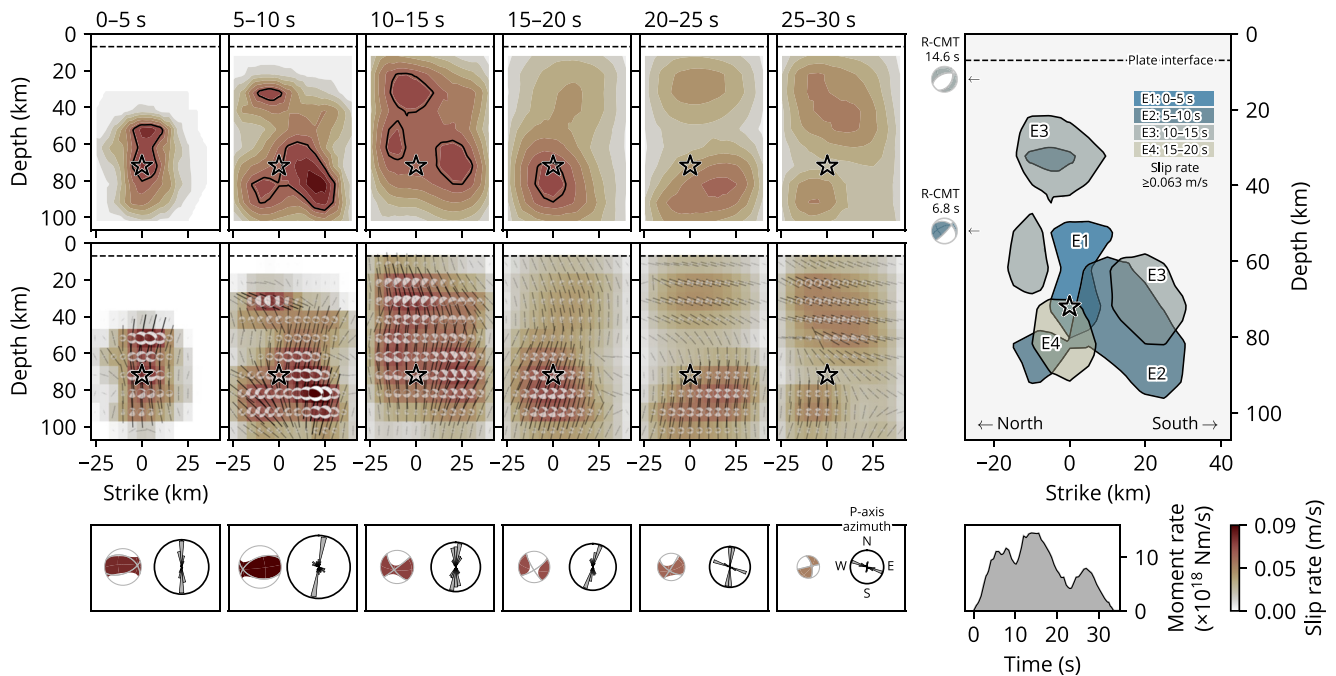


**Figure 3.** Slip evolution. The left panels show the cross sections of the spatiotemporal distribution of slip rate and the resultant moment-rate tensor solution, given in 5 s long windows. The moment tensor is calculated by integrating the slip-rate function for each basis component of moment tensor with respect to the corresponding time window at each subfault. The star represents the hypocenter. The dashed line is the top of the subducting plate (Bassett et al., 2010). The black contour highlights faster slip rates ( $\geq 0.063$  m/s;  $\geq 70\%$  of maximum slip rate). The centroid-moment tensor (CMT) for each time window is shown at the bottom, together with the rose diagram of P-axis azimuths weighted by slip rate. The CMT is calculated by integrating the slip-rate function for each basis component of moment tensor of all the subfaults with respect to the corresponding time window and then constructing a final moment tensor from the integrations by spatially integrating the moment tensors from all the subfaults. All the beach balls of the moment-tensor solution are represented as a lower-hemisphere stereographic projection, not rotated according to the model geometry, but in map view. The right panel summarizes the slip-rate evolution. The color for each episode (E1 to E4) corresponds to the time window. The minor slip-rate events within the final two time windows (20–30 s) are not slipping fast enough to plot a contour on the right panel. R-CMT solutions are also shown at the corresponding depths, with their time shift given relative to the hypocentral time. The right-bottom inset is the total moment-rate function from the finite-fault model.

from south to north. The shallow sub-event can be rather a continuous rupture propagating from deep (50 km) to shallow (30 km) depths during 0–15 s at a speed of  $< 2$  km/s.

#### 4. Intraslab Stress Rotation in Depth

The source process of the 2021 East Cape earthquake could be characterized as multiple episodes rupturing from deep to shallow within the subducted slab (Figure 2). The multi-fault rupture may have caused the small double-couple percentage in the moment tensor solution for the 2021 East Cape earthquake (e.g., 32% in the GCMT solution), which is particularly evident for the deeper rupture domain in our finite-fault solution (Figures 3 and S7 in Supporting Information S1). Such a rupture process would involve a mixture of reverse and strike-slip displacement, which is akin to the 2000  $M_w$  7.9 Enggano intraslab earthquake that ruptured multiple faults at a similar depth leading to a 33% double-couple component in its GCMT solution (Abercrombie et al., 2003). For the shallow slip episode of the 2021 East Cape earthquake, its focal mechanism shows a mixture of the normal faulting with a strike-slip component. The general trend of the aftershock distribution (Figure S2 in Supporting Information S1) suggests that the fault plane striking toward the northeast-southwest direction likely ruptured during the later phase of the earthquake. Although the limited station azimuth coverage could cause an artificially elongated aftershock distribution, the major axis of the uncertainty ellipse of the mainshock relocation, which shares the similar station coverage, is oriented W-E rather than SW-NE (Figure S1 in Supporting Information S1). It is noteworthy that some aftershocks (Dziewonski et al., 1981; Ekström et al., 2012; GeoNet Moment Tensors, 2021; U.S. Geological Survey Earthquake Hazards Program, 2017) share similar focal mechanisms to the shallow rupture episode (Figure S8 in Supporting Information S1). Given the near-trench location of the East Cape earthquake, there is some ambiguity regarding the exact faulting configuration. However, the aftershock distribution indicates that the shallow slip episode likely ruptured a normal fault within the downgoing plate.

Additionally, in the absence of clear shallow slip with a reverse-faulting mechanism, this normal faulting episode likely caused the observed tsunami.

The varying focal mechanisms of the four slip episodes (E1–E4) show the compressional stress orientation (the P-axis orientation) of the East Cape earthquake rotated from the northwest-southeast direction to the north-south direction with a gap in slip and approximate stress transition depth at ~50 km (Figures 2 and 3). The normal faults of the shallow slip episodes striking northeast-southwest agree well with the extension in the upper part of the subducted plate due to the expected plate bending and pulling process (e.g., Ammon et al., 2008; Astiz et al., 1988; Craig et al., 2014; Romeo & Álvarez-Gómez, 2018; Sandiford et al., 2020). Such a bending process seems to have caused most of the background seismicity in this region, which has predominant normal faulting mechanisms (Figure 1; Reyners & McGinty, 1999; Bassett et al., 2010). If the deep slip at 50–100 km depth during the East Cape earthquake was driven by the same bending-related process, we would expect a trench-normal P-axis orientation, which is typical for similar events at other subduction zones, where deep trench-parallel reverse faulting is observed (e.g., Ohta et al., 2011; Okada & Hasegawa, 2003; Todd & Lay, 2013; Ye et al., 2012; Ye et al., 2021). However, the deep slip patches of the East Cape earthquake (E1 and E2 and R-CMT Sub-event 1) have oblique-thrusting mechanisms, resulting in a trench-parallel compression. This perplexing P-axis orientation indicates an additional regional factor that may have modulated the rupture process of the East Cape earthquake.

The interactivity between various faulting episodes is a puzzling part of the East Cape earthquake. Subduction zone earthquakes may involve multiple disconnected subevents with different faulting types that can trigger and interact with each other (Ammon et al., 2008; Hicks & Rietbrock, 2015; Lay et al., 2013, 2020). For the East Cape earthquake, our preferred finite-fault model does not show a continuous rupturing path from the deep to shallow episodes (Figures 2 and 3). The shallow rupture E3 is separated by ~40 km from the deep episodes and started ~5 s later (Figure 3), suggesting an apparent rupture speed of ~8 km/s if the rupture was continuous. Such a rupture speed would be close to the local P-wave speed (Table S1 in Supporting Information S1), which is unlikely. More likely, slip episodes E1 and E2 triggered the following shallow episode E3 due to either the static and/or dynamic stress change from the initial deep rupture. A stress transition or strength contrast within the slab can work as an inhomogeneous barrier (Aki, 1979; Das & Aki, 1977) to smooth propagation from deep to shallow rupture during the East Cape earthquake. Therefore, the rupture evolution of the earthquake may have developed as discontinuous jumps by means of stress triggering (Fischer, Sammis, et al., 2008; Fischer, Peng, & Sammis, 2008; Miyazawa & Mori, 2005; Sleep & Ma, 2008) across the apparent stress/strength barrier between the deep and shallow rupture areas.

Large intraplate earthquakes within the downgoing plate in subduction zones are typically caused either by down-dip bending and unbending of the slab (e.g., Astiz et al., 1988; Craig et al., 2014; Sandiford et al., 2020), the reactivation of major oceanic fabrics, including fracture zones (e.g., Abercrombie et al., 2003; Meng et al., 2012; Yue et al., 2012) or the tearing of the slab (e.g., Tanioka et al., 1995). However, the orientation and rupture complexity of the 2021 East Cape event deviates from these typical events. Two events with apparently similar deep trench-parallel compression in the slab include 2000  $M_w$  7.9 Enggano and 2009  $M_w$  7.6 Padang earthquakes, offshore Sumatra (Abercrombie et al., 2003; Wiseman et al., 2012). However, these events likely ruptured preexisting fabrics in the downgoing plate (Abercrombie et al., 2003), such as fracture zones (Wiseman et al., 2012). Both earthquakes potentially represent the continuation of the diffuse deformation within the Wharton basin, and both consistently ruptured orthogonal fabrics toward the top of the downgoing plate both updip and downdip from the trench, where highly oblique convergence inherently causes a rotated state of the stress in the slab. In contrast, the 2021 East Cape earthquake, which occurred deeper beneath the top of the slab, does not align with the expected oceanic fabric, and is not obviously part of a wider, plate-scale, deformation field, where there is no obvious oblique convergence nor are fracture zones of an orientation consistent with the observed mechanisms subducted (Figure 1). Instead, the rupture processes may represent a unique case, highlighting a different type of stress transition within the subducted slab.

## 5. A Contorted Slab Structure Due to Slab Buoyancy Variations?

A key question is why does this part of the Hikurangi subduction zone exhibit an atypical stress regime, as manifested in the rupture process of the 2021 East Cape earthquake. Slab models of this region (Hayes, 2018; Hayes et al., 2018; Williams et al., 2013) show a homogeneous planar structure (Figure S9 in Supporting Information S1),

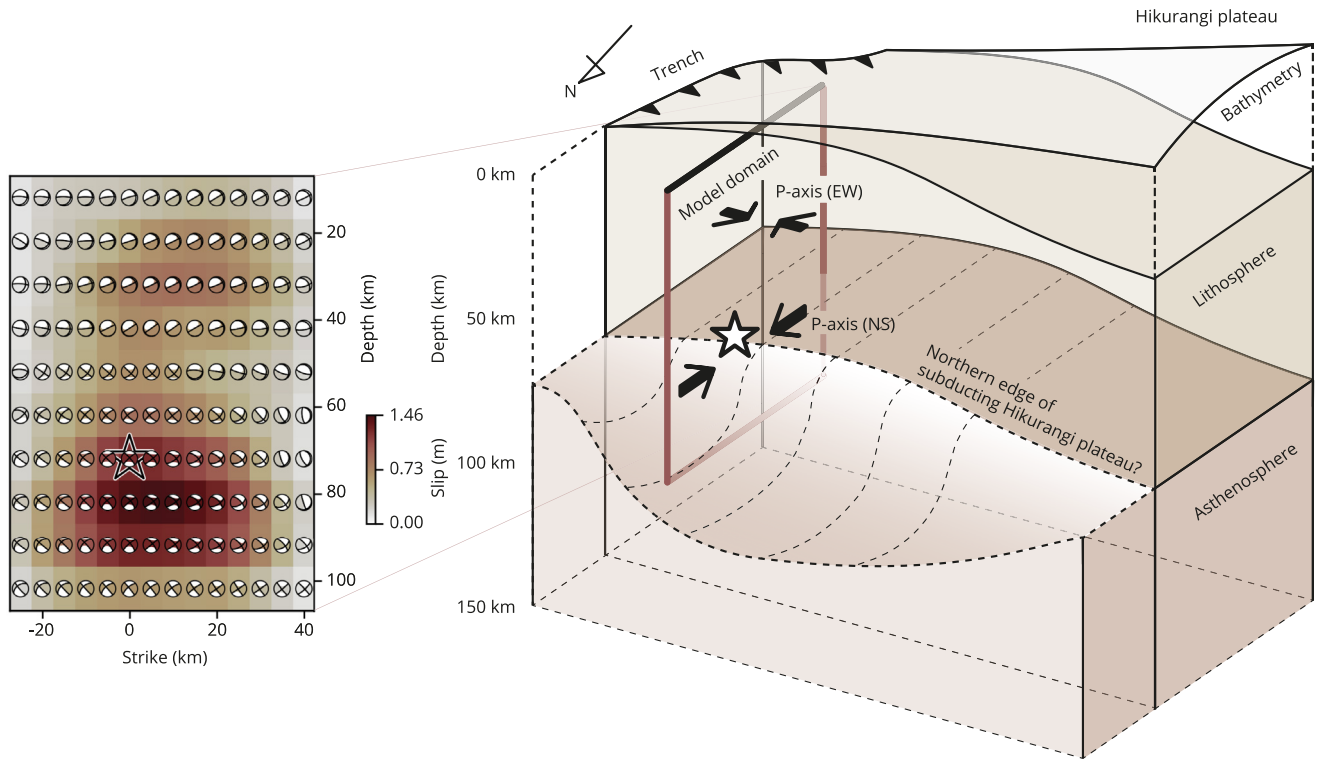


**Figure 4.** Cartoon interpretation of the inferred slab geometry and stress regimes based on our observations of the 2021 East Cape earthquake. The star shows the hypocenter. The arrow shows the compressional axis. The left panel shows the cross-section of our finite-fault solution (Figure S7 in Supporting Information S1).

which would be expected to lead to a trench-normal compression in the deeper part of the slab. However, these slab models are poorly constrained near the East Cape earthquake, largely because of a lack of plate interface thrust earthquakes in the region (Figure 1). The rupture process of the East Cape earthquake therefore potentially offers new insight into the local slab structure.

One possible explanation is that the slab surface warps downward north of the hypocenter, forming a depression at the plate interface (Figure 4). The warping is likely a response to the buoyancy gradients in the subducting plate, which allows the less buoyant parts of the slab to sink more rapidly. The internal stress field from such a slab topology would be complex, leading to strong 3-D stress rotations around the localized downwarp in a manner as shown in the 2021 East Cape earthquake (Figure 2). One contribution to the buoyancy gradients might be the subduction of a large-scale seamount. About 30 km south-west from the epicenter, the Quaternary Ruatoria seamount was obliquely subducted at the margin (Collot et al., 2001; Lewis et al., 1998, 2004), forming the characteristic bathymetry of the Ruatoria indentation (Figure 1). The Ruatoria seamount could deflect and bend the slab, causing the intraslab stress state to rotate from trench-normal compression to trench-parallel compression across the hypocentral area. Numerical models of slab stress in the presence of subducted buoyant features in the oceanic plate support such a stress rotation and lateral spreading mechanism (e.g., Mason et al., 2010). Trench-parallel compression has also been seen in other parts of the Hikurangi subduction zone, for example, Reyners and McGinty (1999) and McGinty et al. (2000) observed some strike-slip seismicity with a trench-parallel compression component, which are beneath or close to the shoreline of the Raukumara Peninsula. Although these earthquakes should reflect the stress state once the plate is already subducted, it is possible they reflect stress heterogeneity due to pervasive seamount subduction along the northern Hikurangi subduction zone (Barker et al., 2009).

An alternative explanation may arise from the location of the East Cape earthquake with respect to the transition between the Kermadec trench and Hikurangi margin, marked by the edge of the Hikurangi plateau, which is represented by a clear bathymetric scarp running along its northern boundary (Davy & Collot, 2000). This transition from the subduction of normal oceanic lithosphere to the north, to the subduction of the thickened oceanic crust



associated with the igneous Hikurangi plateau likely leads to a pronounced, short-wavelength flexural warping at the plateau's edge. The superposition of this N-S flexural stress field in conjunction with the downdip bending stress field could have produced a complex pattern that varies at short-length scales within the subducted slab. Such a heterogeneous stress field may have regulated the rupture process of the East Cape earthquake. The sporadic background seismicity north of the 2021 source region (Figure S16 in Supporting Information S1) might also result from such a complex stress field. It is noteworthy that in 2001, ~80 km northeast of the 2021 event, there was an  $M_w$  7.1 earthquake deep in the Pacific plate (~60 km depth) showing a reverse faulting mechanism with its P-axis oriented perpendicular to the Kermadec trench (Figure S8 in Supporting Information S1), which was likely driven by conventional trench-normal downdip compression. This earthquake suggests that flexural warping due to the subducting Hikurangi plateau does not extend this far to the north.

While there have been many studies on the impact of subducting buoyant features on subduction megathrust coupling and interface seismogenesis (e.g., Nishikawa & Ide, 2014; Wang & Bilek, 2011), there have been far fewer studies that have considered their impact on intraslab seismicity. The rarity of deep intraslab earthquakes in the northern Hikurangi subduction zone makes it difficult to distinguish between the seamount and plateau models of stress rotation. However, it is also possible that both features play a concurrent role, with stress rotations superimposed from both.

## 6. Conclusions

We determined the rupture geometry of the 2021  $M_w$  7.3 East Cape, New Zealand earthquake using a novel finite-fault inversion technique. Our method does not require a-priori knowledge of the fault geometry and can flexibly resolve complex faulting styles in large earthquakes. Therefore, it can illuminate the heterogeneous stress state near the earthquake. We show that the East Cape earthquake involves deep- and shallow-slip episodes, likely rupturing multiple faults with various faulting styles. We find distinct rupture episodes within the shallow (~30 km) and deep (~70 km) parts of the subducted oceanic plate, with distinct mechanisms of normal and a mixture of strike-slip and reverse faulting, respectively. The deep and shallow faulting episodes likely result from the superposition of depth-varying slab-bending stress with more localized trench-parallel lateral variations in flexural stresses. The rotation of P-axes suggests that the intraplate stress state is locally rotated from trench-normal compression to trench-parallel compression. Such a stress rotation in depth requires the slab geometry to change sharply, which may have been induced by a subducted seamount or the additional buoyancy of the Hikurangi plateau. Our study suggests that understanding the generation of intermediate and deep intraslab seismicity requires a detailed treatment of localized variations in slab geometry caused by the subduction of heterogeneous features, such as ocean plateaus and seamounts.

## Conflicts of Interest

The authors declare no conflicts of interest relevant to this study.

## Data Availability Statement

All the materials presented in this paper are archived and available at <https://doi.org/10.5281/zenodo.5720036>. All seismic data were downloaded through the IRIS Wilber 3 system ([https://ds.iris.edu/wilber3/find\\_event](https://ds.iris.edu/wilber3/find_event)) or IRIS Web Services (<https://service.iris.edu>), including the following seismic networks: the GT (Global Telemetered Seismograph Network (USAF/USGS); Albuquerque Seismological Laboratory (ASL)/USGS, 1993); the IC (New China Digital Seismograph Network; Albuquerque Seismological Laboratory (ASL)/USGS, 1992); the IU (Global Seismograph Network (GSN-IRIS/USGS); Albuquerque Seismological Laboratory (ASL)/USGS, 1988); the GE (GEOFON Seismic Network; GEOFON Data Centre, 1993); the AU (Australian National Seismograph Network; Geoscience Australia (GA), 1994); the HK (Hong Kong Seismograph Network; Hong Kong Observatory, 2009); the G (GEOSCOPE; Institut De Physique Du Globe De Paris (IPGP) & Ecole Et Observatoire Des Sciences De La Terre De Strasbourg (EOST), 1982); the NZ (New Zealand National Seismograph Network; Institute of Geological & Nuclear Sciences Ltd (GNS New Zealand), 1988; Petersen et al., 2011); the AI (Antarctic Seismographic Argentinean Italian Network-OGS; Istituto Nazionale Di Oceanografia E Di Geofisica Sperimentale, 1992); the II (IRIS/IDA Seismic Network; Scripps Institution Of Oceanography, 1986);

the C (Chilean National Seismic Network; Universidad de Chile Dept de Geofisica (DGF UChile Chile), 1991); the PS (Pacific21 (ERI/STA) and; University of Tokyo Earthquake Research Institute (Todai ERI Japan), 1989). We used ObsPy (Beyreuther et al., 2010, <https://doi.org/10.5281/zenodo.165135>), Pyrocko (The Pyrocko Developers, 2017, <https://pyrocko.org/>), matplotlib (Hunter, 2007, <https://doi.org/10.5281/zenodo.592536>), Generic Mapping Tools (Wessel & Luis, 2017, <https://doi.org/10.5281/zenodo.3407865>); and Scientific color maps (Crameri, 2018; Crameri et al., 2020, <https://doi.org/10.5281/zenodo.1243862>) for data processing and visualization. The NonLinLoc software used for hypocenter relocation is available at <http://alomax.free.fr/nlloc/>. The Grond software (Heimann et al., 2018) used for *W*-phase CMT inversion is available at <https://pyrocko.org/grond/docs/current/>. The ISOLA software used for R-CMT inversion is available at <http://seismo.geology.upatras.gr/isola/>.

### Acknowledgments

We thank editor Dr. Germán Prieto, associate editor Dr. Ake Fagereng, reviewers Dr. Emily Warren-Smith and Dr. Rachel Abercrombie, and anonymous reviewer for their evaluations and constructive suggestions. We thank Lingsen Meng, Han Bao, Baoning Wu, Richard G. Davy, Lior Suchoy, Fangqin Chen, Rhodri Davies, Tian Feng, Yuqing Xie, Liuwei Xu, and Tong Zhou for the discussions. We are also grateful to John Ristau for discussions on the original GeoNet moment tensor solutions. TJC was supported in this work by the Royal Society under URF/R1\180088. COMET is the NERC Centre for the Observation and Modelling of Earthquakes, Volcanoes, and Tectonics, a partnership between UK Universities and the British Geological Survey. This work was supported by the Grant-in-Aid for Scientific Research (C) 19K04030. The facilities of IRIS Data Services, and specifically the IRIS Data Management Center, were used for access to waveforms, related metadata and/or derived products used in this study. IRIS Data Services are funded through the Seismological Facilities for the Advancement of Geoscience (SAGE) Award of the National Science Foundation under Cooperative Support Agreement EAR-1851048. We also thank the GeoNet data center for making their continuous broadband and strong motion seismic data openly available.

### References

- Abercrombie, R. E., Antolik, M., & Ekström, G. (2003). The June 2000 Mw 7.9 earthquakes south of Sumatra: Deformation in the India-Australia plate. *Journal of Geophysical Research: Solid Earth*, 108(B1), 2018. <https://doi.org/10.1029/2001jb000674>
- Akaïke, H. (1980). Likelihood and the Bayes procedure. *Trabajos de Estadística y de Investigación Operativa*, 31(1), 143–166. <https://doi.org/10.1007/BF02888350>
- Aki, K. (1979). Characterization of barriers on an earthquake fault. *Journal of Geophysical Research*, 84(B11), 6140. <https://doi.org/10.1029/JB084iB11p06140>
- Albuquerque Seismological Laboratory (ASL)/USGS. (1988). *Global Seismograph network (GSN-IRIS/USGS)*. International Federation of Digital Seismograph Networks. <https://doi.org/10.7914/SN/IU>
- Albuquerque Seismological Laboratory (ASL)/USGS. (1992). *New China digital Seismograph network*. International Federation of Digital Seismograph Networks. <https://doi.org/10.7914/SN/IC>
- Albuquerque Seismological Laboratory (ASL)/USGS. (1993). *Global telemetered Seismograph network (USAF/USGS)*. International federation of digital Seismograph networks. <https://doi.org/10.7914/SN/GT>
- Ammon, C. J., Kanamori, H., & Lay, T. (2008). A great earthquake doublet and seismic stress transfer cycle in the central Kuril islands. *Nature*, 451(7178), 561–565. <https://doi.org/10.1038/nature06521>
- Ampuero, J.-P., & Dahlen, F. A. (2005). Ambiguity of the moment tensor. *Bulletin of the Seismological Society of America*, 95(2), 390–400. <https://doi.org/10.1785/0120040103>
- Arai, R., Takahashi, T., Kodaira, S., Kaiho, Y., Nakanishi, A., Fujie, G., & Kaneda, Y. (2016). Structure of the tsunamigenic plate boundary and low-frequency earthquakes in the southern Ryukyu Trench. *Nature Communications*, 7, 1–7. <https://doi.org/10.1038/ncomms12255>
- Astiz, L., Lay, T., & Kanamori, H. (1988). Large intermediate-depth earthquakes and the subduction process. *Physics of the Earth and Planetary Interiors*, 53(1–2), 80–166. [https://doi.org/10.1016/0031-9201\(88\)90138-0](https://doi.org/10.1016/0031-9201(88)90138-0)
- Avouac, J. P., Ayoub, F., Wei, S., Ampuero, J. P., Meng, L., Leprince, S., & Helmerger, D. (2014). The 2013, Mw 7.7 Balochistan earthquake, energetic strike-slip reactivation of a thrust fault. *Earth and Planetary Science Letters*, 391, 128–134. <https://doi.org/10.1016/j.epsl.2014.01.036>
- Barker, D. H., Sutherland, R., Henrys, S., & Bannister, S. (2009). Geometry of the Hikurangi subduction thrust and upper plate, North Island, New Zealand. *Geochemistry, Geophysics, Geosystems*, 10(2), Q02007. <https://doi.org/10.1029/2008GC002153>
- Bassett, D., Kopp, H., Sutherland, R., Henrys, S., Watts, A. B., Timm, C., & Ronde, C. E. J. (2016). Crustal structure of the Kermadec arc from MAN-GO seismic refraction profiles. *Journal of Geophysical Research: Solid Earth*, 121(10), 7514–7546. <https://doi.org/10.1002/2016JB013194>
- Bassett, D., Sutherland, R., Henrys, S., Stern, T., Scherwath, M., Benson, A., & Henderson, M. (2010). Three-dimensional velocity structure of the northern Hikurangi margin, Raukumara, New Zealand: Implications for the growth of continental crust by subduction erosion and tectonic underplating. *Geochemistry, Geophysics, Geosystems*, 11(10), Q10013. <https://doi.org/10.1029/2010GC003137>
- Bell, R., Sutherland, R., Barker, D. H., Henrys, S., Bannister, S., Wallace, L., & Beavan, J. (2010). Seismic reflection character of the Hikurangi subduction interface, New Zealand, in the region of repeated Gisborne slow slip events. *Geophysical Journal International*, 180(1), 34–48. <https://doi.org/10.1111/j.1365-246X.2009.04401.x>
- Beyreuther, M., Barsch, R., Krischer, L., Megies, T., Behr, Y., & Wassermann, J. (2010). ObsPy: A Python toolbox for seismology. *Seismological Research Letters*, 81(3), 530–533. <https://doi.org/10.1785/gssrl.81.3.530>
- Bird, P. (2003). An updated digital model of plate boundaries. *Geochemistry, Geophysics, Geosystems*, 4(3), 1105. <https://doi.org/10.1029/2001GC000252>
- Collot, J. Y., Delteil, J., Lewis, K. B., Davy, B., Lamarche, G., Audru, J. C., & Uruski, C. (1996). From oblique subduction to intra-continental transpression: Structures of the southern Kermadec-Hikurangi margin from multibeam bathymetry, side-scan sonar and seismic reflection. *Marine Geophysical Researches*, 18(2–4), 357–381. <https://doi.org/10.1007/BF00286085>
- Collot, J. Y., Lewis, K., Lamarche, G., & Lallemand, S. (2001). The giant Ruatoria debris avalanche on the northern Hikurangi margin, New Zealand: Result of oblique seamount subduction. *Journal of Geophysical Research: Solid Earth*, 106(B9), 19271–19297. <https://doi.org/10.1029/2001jb900004>
- Craig, T. J., Copley, A., & Jackson, J. (2014). A reassessment of outer-rise seismicity and its implications for the mechanics of oceanic lithosphere. *Geophysical Journal International*, 197(1), 63–89. <https://doi.org/10.1093/gji/ggu013>
- Crameri, F. (2018). Geodynamic diagnostics, scientific visualisation and StagLab 3.0. *Geoscientific Model Development*, 11(6), 2541–2562. <https://doi.org/10.5194/gmd-11-2541-2018>
- Crameri, F., Shephard, G. E., & Heron, P. J. (2020). The misuse of colour in science communication. *Nature Communications*, 11(1), 5444. <https://doi.org/10.1038/s41467-020-19160-7>
- Das, S., & Aki, K. (1977). Fault plane with barriers: A versatile earthquake model. *Journal of Geophysical Research*, 82(36), 5658–5670. <https://doi.org/10.1029/JB082i036p05658>
- Dascher-Cousineau, K., Brodsky, E. E., Lay, T., & Goebel, T. H. W. (2020). What controls variations in aftershock productivity? *Journal of Geophysical Research: Solid Earth*, 125(2), e2019JB018111. <https://doi.org/10.1029/2019JB018111>
- Davey, F. J., Henrys, S., & Lodolo, E. (1997). A seismic crustal section across the East Cape convergent margin, New Zealand. *Tectonophysics*, 269(3–4), 199–215. [https://doi.org/10.1016/S0040-1951\(96\)00165-5](https://doi.org/10.1016/S0040-1951(96)00165-5)

- Davy, B., & Collot, J. Y. (2000). The Rapuhia scarp (northern Hikurangi plateau)-Its nature and subduction effects on the Kermadec trench. *Tectonophysics*, 328(3–4), 269–295. [https://doi.org/10.1016/S0040-1951\(00\)00211-0](https://doi.org/10.1016/S0040-1951(00)00211-0)
- DeMets, C., Gordon, R. G., & Argus, D. F. (2010). Geologically current plate motions. *Geophysical Journal International*, 181(1), 1–80. <https://doi.org/10.1111/j.1365-246X.2009.04491.x>
- Duputel, Z., Agram, P. S., Simons, M., Minson, S. E., & Beck, J. L. (2014). Accounting for prediction uncertainty when inferring subsurface fault slip. *Geophysical Journal International*, 197(1), 464–482. <https://doi.org/10.1093/gji/ggt517>
- Duputel, Z., Rivera, L., Kanamori, H., & Hayes, G. (2012). W phase source inversion for moderate to large earthquakes (1990–2010). *Geophysical Journal International*, 189(2), 1125–1147. <https://doi.org/10.1111/j.1365-246X.2012.05419.x>
- Duputel, Z., Tsai, V. C., Rivera, L., & Kanamori, H. (2013). Using centroid time-delays to characterize source durations and identify earthquakes with unique characteristics. *Earth and Planetary Science Letters*, 374, 92–100. <https://doi.org/10.1016/j.epsl.2013.05.024>
- Dziewonski, A. M., Chou, T.-A., & Woodhouse, J. H. (1981). Determination of earthquake source parameters from waveform data for studies of global and regional seismicity. *Journal of Geophysical Research: Solid Earth*, 86(B4), 2825–2852. <https://doi.org/10.1029/JB086iB04p02825>
- Eberhart-Phillips, D., Bannister, S., Reyners, M., & Henrys, S. (2020). New Zealand Wide model 2.2 seismic velocity and Qs and Qp models for New Zealand. *Zenodo*. <https://doi.org/10.5281/zenodo.3779523>
- Eberhart-Phillips, D., & Reyners, M. (1999). Plate interface properties in the northeast Hikurangi subduction zone, New Zealand, from converted seismic waves. *Geophysical Research Letters*, 26(16), 2565–2568. <https://doi.org/10.1029/1999GL900567>
- Eberhart-Phillips, D., Reyners, M., Bannister, S., Chadwick, M., & Ellis, S. (2010). Establishing a versatile 3-D seismic velocity model for New Zealand. *Seismological Research Letters*, 81(6), 992–1000. <https://doi.org/10.1785/gssrl.81.6.992>
- Ekström, G., Nettles, M., & Dziewoński, A. (2012). The global CMT project 2004–2010: Centroid-moment tensors for 13,017 earthquakes. *Physics of the Earth and Planetary Interiors*, 200–201, 1–9. <https://doi.org/10.1016/j.pepi.2012.04.002>
- Elliott, J. R., Jolivet, R., Gonzalez, P. J., Avouac, J. P., Hollingsworth, J., Searle, M. P., & Stevens, V. L. (2016). Himalayan megathrust geometry and relation to topography revealed by the Gorkha earthquake. *Nature Geoscience*, 9(2), 174–180. <https://doi.org/10.1038/ngeo2623>
- Fischer, A. D., Peng, Z., & Sammis, C. G. (2008). Dynamic triggering of high-frequency bursts by strong motions during the 2004 Parkfield earthquake sequence. *Geophysical Research Letters*, 35(12), L12305. <https://doi.org/10.1029/2008GL033905>
- Fischer, A. D., Sammis, C. G., Chen, Y., & Teng, T.-L. (2008). Dynamic triggering by strong-motion P and S waves: Evidence from the 1999 Chi-Chi, Taiwan, earthquake. *Bulletin of the Seismological Society of America*, 98(2), 580–592. <https://doi.org/10.1785/0120070155>
- Floyd, M. A., Walters, R. J., Elliott, J. R., Funning, G. J., Svarc, J. L., Murray, J. R., & Wright, T. J. (2016). Spatial variations in fault friction related to lithology from rupture and afterslip of the 2014 South Napa, California, earthquake. *Geophysical Research Letters*, 43(13), 6808–6816. <https://doi.org/10.1002/2016GL069428>
- Fukuda, J., & Johnson, K. M. (2008). A fully Bayesian inversion for spatial distribution of fault slip with objective smoothing. *Bulletin of the Seismological Society of America*, 98(3), 1128–1146. <https://doi.org/10.1785/0120070194>
- GEOFON Data Centre. (1993). GEOFON seismic network. *Deutsches GeoForschungsZentrum GFZ*. <https://doi.org/10.14470/TR560404>
- GeoNet. (2021). *GeoNet earthquake catalog*. Retrieved from [https://www.geonet.org.nz/data/types/eq\\_catalogue](https://www.geonet.org.nz/data/types/eq_catalogue)
- GeoNet Moment Tensors. (2021). *GeoNet moment tensors*. Retrieved from <https://github.com/GeoNet/data/tree/main/moment-tensor>
- GeoNet News. (2021). *Friday 5 March Tsunami: What happened and what did you see?* Retrieved from <https://www.geonet.org.nz/news/1gvqV0oHGIULbydSQD8W1Y>
- Geoscience Australia (GA). (1994). *Australian national Seismograph network (ANSN)*. Retrieved from <https://www.fdsn.org/networks/detail/AU/>
- Gomberg, J., & Bodin, P. (2021). The productivity of cascadia aftershock sequences. *Bulletin of the Seismological Society of America*, 111(3), 1–14. <https://doi.org/10.1785/0120200344>
- Hamling, I. J., Hreinsdóttir, S., Clark, K., Elliott, J., Liang, C., Fielding, E., & Stirling, M. (2017). Complex multifault rupture during the 2016 Mw 7.8 Kaikōura earthquake, New Zealand. *Science*, 356(6334). <https://doi.org/10.1126/science.aam7194>
- Hayes, G. P. (2018). *Slab2-A comprehensive subduction zone geometry model*. U.S. Geological Survey data release. <https://doi.org/10.5066/F7PV6JNV>
- Hayes, G. P., Moore, G. L., Portner, D. E., Hearne, M., Flamme, H., Furtney, M., & Smoczyk, G. M. (2018). Slab2, a comprehensive subduction zone geometry model. *Science*, 362(6410), 58–61. <https://doi.org/10.1126/science.aat4723>
- Heimann, S., Isken, M., Kühn, D., Sudhaus, H., Steinberg, A., Vasyura-Bathke, H., & Dahm, T. (2018). *GronD-A probabilistic earthquake source inversion framework*. <https://doi.org/10.5880/GFZ.2.1.2018.003>
- Henrys, S., Reyners, M., Pecher, I., Bannister, S., Nishimura, Y., & Maslen, G. (2006). Kinking of the subducting slab by escarpment normal faulting beneath the North Island of New Zealand. *Geology*, 34(9), 777–780. <https://doi.org/10.1130/G22594.1>
- Hicks, S. P., Okuwaki, R., Steinberg, A., Rychert, C. A., Harmon, N., Abercrombie, R. E., & Sudhaus, H. (2020). Back-propagating super-shear rupture in the 2016 Mw 7.1 Romanche transform fault earthquake. *Nature Geoscience*, 13(9), 647–653. <https://doi.org/10.1038/s41561-020-0619-9>
- Hicks, S. P., & Rietbrock, A. (2015). Seismic slip on an upper-plate normal fault during a large subduction megathrust rupture. *Nature Geoscience*, 8(12), 955–960. <https://doi.org/10.1038/ngeo2585>
- Hong Kong Observatory. (2009). *Hong Kong Seismograph network*. Retrieved from [http://www.hko.gov.hk/gts/quake/sp\\_seismo\\_network\\_intro\\_e.htm](http://www.hko.gov.hk/gts/quake/sp_seismo_network_intro_e.htm)
- Hunter, J. D. (2007). Matplotlib: A 2D graphics environment. *Computing in Science & Engineering*, 9(3), 90–95. <https://doi.org/10.1109/MCSE.2007.55>
- Institut De Physique Du Globe De Paris (IPGP), & Ecole Et Observatoire Des Sciences De La Terre De Strasbourg (EOST). (1982). *GEOSCOPE, French Global Network of broad band seismic stations*. Institut de physique du globe de Paris (IPGP). <https://doi.org/10.18715/GEOSCOPE.G>
- Institute of Geological & Nuclear Sciences Ltd (GNS New Zealand). (1988). *New Zealand national Seismograph network*. Retrieved from <https://www.fdsn.org/networks/detail/NZ/>
- International Seismological Centre. (2021). *On-line Bulletin*. <https://doi.org/10.31905/D808B830>
- Istituto Nazionale Di Oceanografia E Di Geofisica Sperimentale. (1992). *Antarctic seismographic Argentinean Italian network-OGS*. International Federation of Digital Seismograph Networks. <https://doi.org/10.7914/SN/AI>
- Kaneko, Y., Ito, Y., Chow, B., Wallace, L. M., Tape, C., Grapenthin, R., & Hino, R. (2019). Ultra-long duration of seismic ground motion arising from a thick, low-velocity sedimentary wedge. *Journal of Geophysical Research: Solid Earth*, 124(10), 10347–10359. <https://doi.org/10.1029/2019JB017795>
- Kikuchi, M., & Kanamori, H. (1991). Inversion of complex body waves-III. *Bulletin of the Seismological Society of America*, 81(6), 2335–2350. <https://doi.org/10.1785/bssa0810062335>

- Lay, T., Duputel, Z., Ye, L., & Kanamori, H. (2013). The December 7, 2012 Japan Trench intraplate doublet (Mw 7.2, 7.1) and interactions between near-trench intraplate thrust and normal faulting. *Physics of the Earth and Planetary Interiors*, 220, 73–78. <https://doi.org/10.1016/j.pepi.2013.04.009>
- Lay, T., Ye, L., Wu, Z., & Kanamori, H. (2020). Macrofracturing of oceanic lithosphere in complex large earthquake sequences. *Journal of Geophysical Research: Solid Earth*, 125(10), 1–21. <https://doi.org/10.1029/2020JB020137>
- Lewis, K. B., Collot, J. Y., & Lallemand, S. E. (1998). The dammed Hikurangi trough: A channel-fed trench blocked by subducting seamounts and their wake avalanches (New Zealand-France GeodyNZ project). *Basin Research*, 10(4), 441–468. <https://doi.org/10.1046/j.1365-2117.1998.00080.x>
- Lewis, K. B., Lallemand, S. E., & Carter, L. (2004). Collapse in a quaternary shelf basin off East Cape, New Zealand: Evidence for passage of a subducted seamount inboard of the ruatoria giant avalanche. *New Zealand Journal of Geology and Geophysics*, 47(3), 415–429. <https://doi.org/10.1080/00288306.2004.9515067>
- Mason, W. G., Moresi, L., Betts, P. G., & Miller, M. S. (2010). Three-dimensional numerical models of the influence of a buoyant oceanic plateau on subduction zones. *Tectonophysics*, 483(1–2), 71–79. <https://doi.org/10.1016/j.tecto.2009.08.021>
- McGinty, P., Reyners, M., & Robinson, R. (2000). Stress directions in the shallow part of the Hikurangi subduction zone, New Zealand, from the inversion of earthquake first motions. *Geophysical Journal International*, 142(2), 339–350. <https://doi.org/10.1046/j.1365-246X.2000.00155.x>
- Meng, L., Ampuero, J. P., Stock, J., Duputel, Z., Luo, Y., & Tsai, V. C. (2012). Earthquake in a maze: Compressional rupture branching during the 2012 Mw 8.6 Sumatra earthquake. *Science*, 337(6095), 724–726. <https://doi.org/10.1126/science.1224030>
- Minson, S. E., Simons, M., & Beck, J. L. (2013). Bayesian inversion for finite fault earthquake source models I-theory and algorithm. *Geophysical Journal International*, 194(3), 1701–1726. <https://doi.org/10.1093/gji/ggt180>
- Mitchell, J. S., Mackay, K. A., Neil, H. L., Mackay, E. J., Pallentin, A., & Notman, P. (2012). *Undersea New Zealand, 1: 5,000,000. NIWA Chart, Misc. Ser.* (Vol. 92). Retrieved from <https://niwa.co.nz/our-science/oceans/bathymetry/further-information>
- Miyazawa, M., & Mori, J. (2005). Detection of triggered deep low-frequency events from the 2003 Tokachi-oki earthquake. *Geophysical Research Letters*, 32(10), 1–4. <https://doi.org/10.1029/2005GL022539>
- Mochizuki, K., Henrys, S., Hajjima, D., Warren-Smith, E., & Fry, B. (2021). Seismicity and velocity structure in the vicinity of repeating slow slip earthquakes, northern Hikurangi subduction zone, New Zealand. *Earth and Planetary Science Letters*, 563, 116887. <https://doi.org/10.1016/j.epsl.2021.116887>
- Nishikawa, T., & Ide, S. (2014). Earthquake size distribution in subduction zones linked to slab buoyancy. *Nature Geoscience*, 7(12), 904–908. <https://doi.org/10.1038/ngeo2279>
- Ohta, Y., Miura, S., Ohzono, M., Kita, S., Linuma, T., Demachi, T., & Umino, N. (2011). Large intraslab earthquake (2011 April 7, M 7.1) after the 2011 off the Pacific coast of Tohoku Earthquake (M 9.0): Coseismic fault model based on the dense GPS network data. *Earth Planets and Space*, 63(12), 1207–1211. <https://doi.org/10.5047/eps.2011.07.016>
- Okada, T., & Hasegawa, A. (2003). The M7.1 May 26, 2003 off-shore Miyagi Prefecture Earthquake in northeast Japan: Source process and aftershock distribution of an intra-slab event. *Earth Planets and Space*, 55(12), 731–739. <https://doi.org/10.1186/BF03352482>
- Okuwaki, R., Hirano, S., Yagi, Y., & Shimizu, K. (2020). Inchworm-like source evolution through a geometrically complex fault fueled persistent supershear rupture during the 2018 Palu Indonesia earthquake. *Earth and Planetary Science Letters*, 547, 116449. <https://doi.org/10.1016/j.epsl.2020.116449>
- Page, M. T., van Der Elst, N., Hardebeck, J., Felzer, K., & Michael, A. J. (2016). Three ingredients for improved global aftershock forecasts: Tectonic region, time-dependent catalog incompleteness, and intersequence variability. *Bulletin of the Seismological Society of America*, 106(5), 2290–2301. <https://doi.org/10.1785/0120160073>
- Petersen, T., Gledhill, K., Chadwick, M., Gale, N. H., & Ristau, J. (2011). The New Zealand national Seismograph network. *Seismological Research Letters*, 82(1), 9–20. <https://doi.org/10.1785/gssrl.82.1.9>
- Ragon, T., Sladen, A., & Simons, M. (2018). Accounting for uncertain fault geometry in earthquake source inversions—I: Theory and simplified application. *Geophysical Journal International*, 214(2), 1174–1190. <https://doi.org/10.1093/gji/ggy187>
- Ranero, C. R., Villaseñor, A., Morgan, J. P., & Weinrebe, W. (2005). Relationship between bend-faulting at trenches and intermediate-depth seismicity. *Geochemistry, Geophysics, Geosystems*, 6(12), Q12002. <https://doi.org/10.1029/2005GC000997>
- Reyners, M., Eberhart-Phillips, D., Stuart, G., & Nishimura, Y. (2006). Imaging subduction from The trench to 300 km depth beneath the central North Island, New Zealand, with Vp and Vp/Vs. *Geophysical Journal International*, 165(2), 565–583. <https://doi.org/10.1111/j.1365-246X.2006.02897.x>
- Reyners, M., & McGinty, P. (1999). Shallow subduction tectonics in the Raukumara Peninsula, New Zealand, as illuminated by earthquake focal mechanisms. *Journal of Geophysical Research: Solid Earth*, 104(B2), 3025–3034. <https://doi.org/10.1029/1998JB900081>
- Romeo, I., & Álvarez-Gómez, J. A. (2018). Lithospheric folding by flexural slip in subduction zones as source for reverse fault intraslab earthquakes. *Scientific Reports*, 8(1), 1–9. <https://doi.org/10.1038/s41598-018-19682-7>
- Sandiford, D., Moresi, L., Sandiford, M., & Yang, T. (2019). Geometric controls on flat slab seismicity. *Earth and Planetary Science Letters*, 527, 115787. <https://doi.org/10.1016/j.epsl.2019.115787>
- Sandiford, D., Moresi, L. M., Sandiford, M., Farrington, R., & Yang, T. (2020). The fingerprints of flexure in slab seismicity. *Tectonics*, 39(8). <https://doi.org/10.1029/2019TC005894>
- Scripps Institution Of Oceanography. (1986). *IRIS/IDA seismic network*. International Federation of Digital Seismograph Networks. <https://doi.org/10.7914/SN/II>
- Shimizu, K., Yagi, Y., Okuwaki, R., & Fukahata, Y. (2020). Development of an inversion method to extract information on fault geometry from teleseismic data. *Geophysical Journal International*, 220(2), 1055–1065. <https://doi.org/10.1093/gji/ggz496>
- Shimizu, K., Yagi, Y., Okuwaki, R., & Fukahata, Y. (2021). Construction of fault geometry by finite-fault inversion of teleseismic data. *Geophysical Journal International*, 224(2), 1003–1014. <https://doi.org/10.1093/gji/ggaa501>
- Simons, M., Fialko, Y., & Rivera, L. (2002). Coseismic deformation from the 1999 Mw 7.1 Hector Mine, California, earthquake as inferred from InSAR and GPS observations. *Bulletin of the Seismological Society of America*, 92(4), 1390–1402. <https://doi.org/10.1785/0120000933>
- Sippl, C., Schurr, B., Asch, G., & Kummerow, J. (2018). Seismicity structure of the Northern Chile forearc from >100,000 double-difference relocated hypocenters. *Journal of Geophysical Research: Solid Earth*, 123(5), 4063–4087. <https://doi.org/10.1002/2017JB015384>
- Sleep, N. H., & Ma, S. (2008). Production of brief extreme ground acceleration pulses by nonlinear mechanisms in the shallow subsurface. *Geochemistry, Geophysics, Geosystems*, 9(3), Q03008. <https://doi.org/10.1029/2007GC001863>
- Tadapansawut, T., Okuwaki, R., Yagi, Y., & Yamashita, S. (2021). Rupture process of the 2020 Caribbean earthquake along the Oriente Transform Fault, involving supershear rupture and geometric complexity of fault. *Geophysical Research Letters*, 48(1), 1–9. <https://doi.org/10.1029/2020GL090899>
- Tanioka, Y., Ruff, L., & Satake, K. (1995). The great Kurile Earthquake of October 4, 1994 tore the slab. *Geophysical Research Letters*, 22(13), 1661–1664. <https://doi.org/10.1029/95GL01656>



- The Pyrocko Developers. (2017). *Pyrocko: A versatile seismology toolkit for Python*. <https://doi.org/10.5880/GFZ.2.1.2017.001>
- Todd, E. K., & Lay, T. (2013). The 2011 Northern Kermadec earthquake doublet and subduction zone faulting interactions. *Journal of Geophysical Research: Solid Earth*, *118*(1), 249–261. <https://doi.org/10.1029/2012JB009711>
- Universidad de Chile Dept de Geofisica (DGF UChile Chile). (1991). *Chilean National Seismic Network*. Retrieved from <https://www.fdsn.org/networks/detail/C/>
- University of Tokyo Earthquake Research Institute (Todai ERI Japan). (1989). *Pacific21 (ERI/STA)*. Retrieved from <https://www.fdsn.org/networks/detail/PS/>
- U.S. Geological Survey Earthquake Hazards Program. (2017). *Advanced national seismic system (ANSS) comprehensive catalog of earthquake events and products*. <https://doi.org/10.5066/F7MS3QZH>
- Wallace, L. M., Reyners, M., Cochran, U., Bannister, S., Barnes, P. M., Berryman, K., & Power, W. (2009). Characterizing the seismogenic zone of a major plate boundary subduction thrust: Hikurangi Margin, New Zealand. *Geochemistry, Geophysics, Geosystems*, *10*(10), Q10006. <https://doi.org/10.1029/2009GC002610>
- Wang, K., & Bilek, S. L. (2011). Do subducting seamounts generate or stop large earthquakes? *Geology*, *39*(9), 819–822. <https://doi.org/10.1130/G31856.1>
- Wessel, P., & Luis, J. F. (2017). The GMT/MATLAB toolbox. *Geochemistry, Geophysics, Geosystems*, *18*(2), 811–823. <https://doi.org/10.1002/2016GC006723>
- Wiens, D. A. (2001). Seismological constraints on the mechanism of deep earthquakes: Temperature dependence of deep earthquake source properties. *Physics of the Earth and Planetary Interiors*, *127*(1–4), 145–163. [https://doi.org/10.1016/S0031-9201\(01\)00225-4](https://doi.org/10.1016/S0031-9201(01)00225-4)
- Williams, C. A., Eberhart-Phillips, D., Bannister, S., Barker, D. H., Henrys, S., Reyners, M., & Sutherland, R. (2013). Revised interface geometry for the hikurangi subduction zone, New Zealand. *Seismological Research Letters*, *84*(6), 1066–1073. <https://doi.org/10.1785/0220130035>
- Wiseman, K., Banerjee, P., Bürgmann, R., Sieh, K., Dreger, D. S., & Hermawan, I. (2012). Source model of the 2009 Mw 7.6 Padang intraslab earthquake and its effect on the Sunda megathrust. *Geophysical Journal International*, *190*(3), 1710–1722. <https://doi.org/10.1111/j.1365-246X.2012.05600.x>
- Yabuki, T., & Matsu'ura, M. (1992). Geodetic data inversion using a Bayesian information criterion for spatial distribution of fault slip. *Geophysical Journal International*, *109*(2), 363–375. <https://doi.org/10.1111/j.1365-246X.1992.tb00102.x>
- Yagi, Y., & Fukahata, Y. (2011). Introduction of uncertainty of Green's function into waveform inversion for seismic source processes. *Geophysical Journal International*, *186*(2), 711–720. <https://doi.org/10.1111/j.1365-246X.2011.05043.x>
- Yamashita, S., Yagi, Y., Okuwaki, R., Shimizu, K., Agata, R., & Fukahata, Y. (2021). Consecutive ruptures on a complex conjugate fault system during the 2018 Gulf of Alaska earthquake. *Scientific Reports*, *11*(1), 5979. <https://doi.org/10.1038/s41598-021-85522-w>
- Ye, L., Lay, T., Bai, Y., Cheung, K. F., & Kanamori, H. (2017). The 2017 Mw 8.2 Chiapas, Mexico, earthquake: Energetic slab detachment. *Geophysical Research Letters*, *44*(23), 11824–11832. <https://doi.org/10.1002/2017GL076085>
- Ye, L., Lay, T., & Kanamori, H. (2012). Intraplate and interplate faulting interactions during the August 31, 2012, Philippine Trench earthquake (Mw 7.6) sequence. *Geophysical Research Letters*, *39*(24), 1–6. <https://doi.org/10.1029/2012GL054164>
- Ye, L., Lay, T., & Kanamori, H. (2021). The 25 March 2020 Mw 7.5 Paramushir, northern Kuril Islands earthquake and major (Mw  $\geq$ 7.0) near-trench intraplate compressional faulting. *Earth and Planetary Science Letters*, *556*(March 2020), 116728. <https://doi.org/10.1016/j.epsl.2020.116728>
- Yue, H., Lay, T., & Koper, K. D. (2012). En échelon and orthogonal fault ruptures of the 11 April 2012 great intraplate earthquakes. *Nature*, *490*(7419), 245–249. <https://doi.org/10.1038/nature11492>

## References From the Supporting Information

- Bormann, P. (2012). New manual of seismological observatory practice (NMSOP-2). IASPEI, GFZ Ger. *Research Centre for Geosciences*. <https://doi.org/10.2312/GFZ.NMSOP-2>
- Kennett, B. L., Engdahl, E. R., & Buland, R. (1995). Constraints on seismic velocities in the Earth from traveltimes. *Geophysical Journal International*, *122*(1), 108–124. <https://doi.org/10.1111/j.1365-246X.1995.tb03540.x>
- Laske, G., Masters, T. G., Ma, Z., & Pasyanos, M. (2013). Update on CRUST1.0-A 1-degree global model of Earth's crust. *Geophysical Research Abstracts*, *15*. Retrieved from <https://iggppweb.ucsd.edu/~gabi/crust1.html>
- Lomax, A., Michelini, A., & Curtis, A. (2009). Earthquake location, direct, global-search methods BT-Encyclopedia of complexity and systems science. *Encyclopedia of Complexity and Systems Science*, 2449–2473. [https://doi.org/10.1007/978-0-387-30440-3\\_150](https://doi.org/10.1007/978-0-387-30440-3_150)
- Lomax, A., Virieux, J., Volant, P., & Berge-Thierry, C. (2000). Probabilistic earthquake location in 3D and layered models BT-Advances in seismic event location. In C. H. Thurber, & N. Rabinowitz (Eds.), (pp. 101–134). Springer Netherlands. [https://doi.org/10.1007/978-94-015-9536-0\\_5](https://doi.org/10.1007/978-94-015-9536-0_5)
- Okuwaki, R., Yagi, Y., Aránguiz, R., González, J., & González, G. (2016). Rupture process during the 2015 Illapel, Chile earthquake: Zigzag-Along-Dip rupture episodes. *Pure and Applied Geophysics*, *173*(4), 1011–1020. <https://doi.org/10.1007/s00024-016-1271-6>
- Sokos, E. N., & Zahradnik, J. (2008). ISOLA a Fortran code and a Matlab GUI to perform multiple-point source inversion of seismic data. *Computers & Geosciences*, *34*(8), 967–977. <https://doi.org/10.1016/j.cageo.2007.07.005>
- Vallée, M. (2013). Source time function properties indicate a strain drop independent of earthquake depth and magnitude. *Nature Communications*, *4*, 1–6. <https://doi.org/10.1038/ncomms3606>
- Vallée, M., Charléty, J., Ferreira, A. M., Delouis, B., & Vergoz, J. (2011). SCARDEC: A new technique for the rapid determination of seismic moment magnitude, focal mechanism and source time functions for large earthquakes using body-wave deconvolution. *Geophysical Journal International*, *184*(1), 338–358. <https://doi.org/10.1111/j.1365-246X.2010.04836.x>